Geophysical Research Letters

Supporting Information for

Electrical resistivity anomalies offshore a carbonate coastline: Evidence for freshened groundwater?

Amir Haroon[1], Aaron Micallef[1,2], Marion Jegen[1], Katrin Schwalenberg[3], Jens Karstens[1], Christian Berndt[1], Xavier Garcia[4], Michel Kuehn[1], Enzo Rizzo[5], Nicoletta Chiara Fusi[6], Chibuzo Valeria Ahaneku [2,7], Lorenzo Petronio[8], Zahra Faghih[1], Bradley A. Weymer[1], Michele De Biase[9], Francesco Chidichimo[9]

[1] Helmholtz Centre for Ocean Research, GEOMAR, Kiel, Germany
[2] Marine Geology & Seafloor Surveying, Department of Geosciences, University of Malta, Malta
[3] Federal Institute for Geosciences and Natural Resources (BGR), Germany
[4] Institute of Marine Science, CSIC, Barcelona, Spain
[5] Dipartimento di Fisica e Scienze della Terra, University of Ferrara, Ferrara, Italy
[6] Earth and Environmental Sciences Department; University of Milano-Bicocca, Italy
[7] Department of Geological Sciences, Nnamdi Azikiwe University, Awka, Anambra State, Nigeria
[8] Istituto Nazionale di Oceanografia e di Geofisica Sperimentale (OGS), Trieste, Italy
[9] Department of Environmental Engineering, University of Calabria, Rende, Italy

Contents of this file

S1. Core Log Resistivity Measurements

Correlating laboratory resistivity measurements with geophysical resistivity models helps constrain the geology and lithology of the survey area. In this paper, we measured seven core samples, one for each limestone formation outcropping on Malta and Gozo: Upper Coralline (Tal Pitkal and Mtarfa), Lower Coralline (Attard and Xlendi), and Globigerina (Upper, Middle, and Lower). The blue markers in Figure 1 of the manuscript show the locations of where the samples were obtained. These are analysed to determine realistic resistivity ranges for each lithological unit to inform the interpretation of the CSEM inversion models. Here, we used three different saturation states, (dry, water saturated (1.3

S/m) and seawater saturated (5 S/m)). Electrical resistivity (ρ) is an intrinsic electrical material property, independent of a material's size and shape, that characterizes the flow of electric current through the material. The dominant factors that determine a sample's electrical resistivity are clay content, porosity, pore water salinity and degree of saturation. In the absence of clay, dry materials are typically more resistive than wet materials, and material saturated with saline water will be even more conductive. Each core is sampled in the frequency range of 20 Hz to 0.5×10^6 Hz.

All measurements were made using a Wayne Kerr Electronics Precision Impedance Analyzers (6440B model), which provide precise and fast testing of components at frequencies up to 0.5×10^6 Hz. The LCR impedance measurements were carried out using a two-electrode measurement. The LCR (Inductance (L), Capacitance (C), and Resistance (R)) meter sweeps through a series of measurement frequencies and stores the frequency-dependent impedance, resistance, and phase values. We apply testing voltage of 1 Vrms at constant room temperature (18 ^{0}C). The sample was enclosed between two copper electrodes and a Teflon cylinder. For each sample, we measured the impedance (Z) at different frequencies. Z is an imaginary quantity, where the real part describes the resistance, and the imaginary part the reactance. Thus, taking in account the amplitudes and the phases (which is the angle between the real and imaginary component) we estimate the resistance (R) by R = |Z|cos(phase). Taking the sample size into account, we can derive the electrical resistivity of all samples.

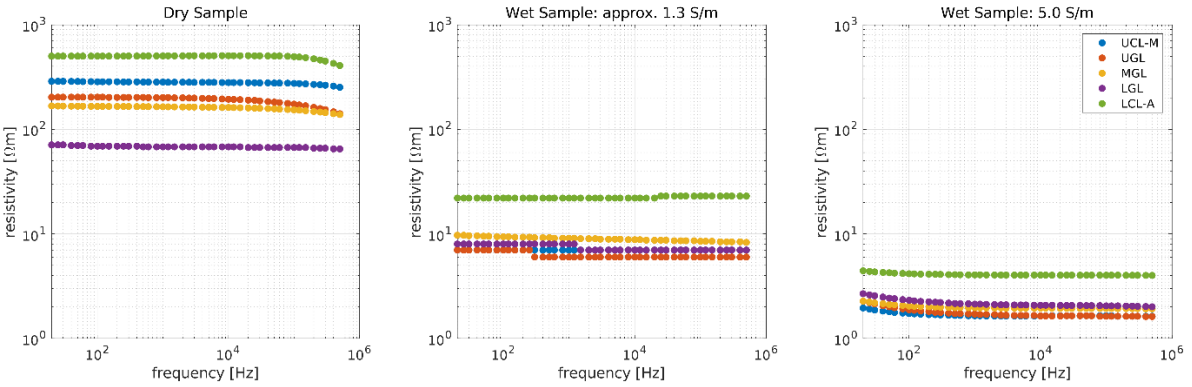

Figure S1: Electrical resistivity measured at various frequencies for (a) dry samples, (b) wet samples saturated with 1.3 S/m water, and (c) wet samples saturated with 5 S/m salt water. The line colours correspond to the different core samples. Note that UCL-T and LCL-X are excluded since core samples were only poorly saturated with fluid and did not allow for trustworthy measurements.

The three graphs in Figure S1 illustrate the electrical resistivity values calculated by LCR impedance measurements for all samples excluding LCL-X and UCL-T. These two samples could not be sufficiently saturated to provide trustworthy results. The data show high electrical resistivity values in dry conditions (left) and decreased electrical resistivities in seawater-saturated conditions (right). Generally, the electrical resistivity of the investigated samples shows only slight frequency dependency. The graphs highlight the electrical resistivity range of the Maltese formations with values between 70 Ωm to 500 Ωm in dry conditions and between values of 1.6 Ωm to 4.5 when saturated with seawater. The OFG prospects Globigerina and LCL members have resistivities between 2.2-2.6 Ωm and approximately 4.5 Ωm, respectively. These lie below the values obtained for the resistive anomalies R1-R4 in the CSEM inversion models.

S2. Core Log Porosity Measurements

Intact cores were scanned with an industrial microCT (Bir/Actis 130/150). MicroCT images (voxel size: 26 µm) were subsequently segmented and binarized (rock and voids) using Avizo software (Thermofisher). We conducted a statistical analysis of the pore space and derived total porosity for each sample. In addition to measuring the porosity using microCT and a triaxial cell, we computed a porosity estimation based on volume ratios before and after saturation, taking a saltwater density of 1.020 g/cm3. For all samples, the Vw/Vs porosity estimations are larger compared to microCT and triaxial cell. Additionally, the computed porosities fit into the ranges suggested by preceding literature (e.g. Pedley et al. (1976); Stuart et al (2010); Cassar (2010); Cooke et al. (2018); Gatt (2012); Bakalowicz & Mangion (2003) Sapiano et al. (2017a, b)). Consequently, we have chosen to use only these porosities for the following considerations to determine the Archie parameters. MicroCT images are displayed in Figure S2 and are qualitatively used to describe the pore space characteristics of each sample in the main text.

Table S1: *Porosity and permeability measurements made on core samples.*

	Diameter (mm)	Height (mm)	Volume (cm^3)	Weight (g)	Density (g/cm^3)	Weight after saturation process (g)	Water content (g)	Porosity (V_w/V_s)	Porosity (Triax)	Porosity (microCT)
Upper Coralline - Tal Pitkal	38.20	73.90	84.70	220.12	2.60	221.62	1.50	0.02	0.01	0.01
Upper Coralline - Mtarfa	37.50	77.60	85.71	151.57	1.77	177.59	26.02	0.30	0.17	0.08
Blue Clay	70.00	69.00	265.54	498.82	1.88	Impermeable				
Upper Globigerina	37.70	65.10	72.67	111.14	1.53	137.50	26.36	0.36	0.21	0.04
Middle Globigerina	37.60	77.60	86.16	141.85	1.65	167.56	25.71	0.29	0.18	0.01
Lower Globigerina	37.70	69.20	77.25	138.43	1.79	159.62	21.19	0.27	0.15	0.03
Lower Coralline Xlendi	38.10	74.00	84.37	214.26	2.54	215.37	1.11	0.01	0.01	0.03
Lower Coralline Attard	37.60	71.00	78.84	165.09	2.09	180.35	15.26	0.19	0.09	0.01

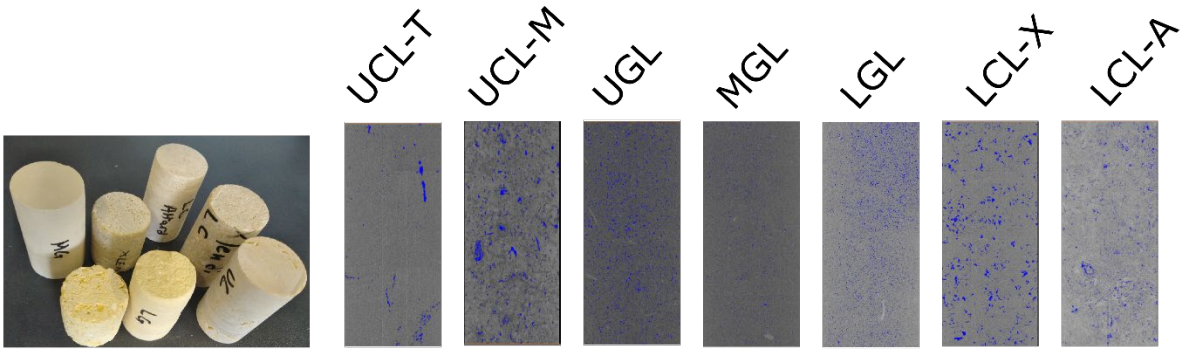

Figure S2: Core samples and processed CT images for each sample. The blue colouring in each image shows the pore space distribution for each sample.

The two members of UCL are characterized by very different hydraulic conductivity. Tal-Pitkal is completely impermeable in triaxial test, microCT images reveal a prevalence of big elongated pores not interconnected. On the other hand, Mtarfa is the most permeable member of the whole stratigraphic sequence; pores are related to fossil abundance and shell dissolution. Blue Clay (not shown here) is characterized by low hydraulic conductivity, due to the clayey-silty grain size. GL members are characterized by evenly distributed round pores, smaller in Lower and Medium GL than Upper GL. Similarly, to UCL, LCL is characterized by very different porosity and hydraulic conductivity. The upper member (LCL-X) is completely impermeable in triaxial test. MicroCT images reveal big irregular pores with no connections. On the contrary LCL-A is permeable with pores concentrated in fossils, such as empty gastropods chambers or due to shell dissolution.

S3. Archie's Equation

To determine the resistivity of each limestone under marine conditions, the samples were saturated with seawater (ρ_w=0.2 Ωm). Resistivities were measured as a function of frequency for different saturation levels. For sediments and sandstones, the relationship between bulk resistivity, porosity, and pore fluid saturation can be described by Archie's empirical equation (Archie, 1942):

$$\rho_{bulk} = S^{-n}\phi^{-m}\rho_w$$

where n~2 and *m* is a constant that ranges from 1.5-2.5. We aim to determine a value for *m* based on the laboratory resistivity and porosity measurements, which we use in the discussion to interpret the CSEM resistivity models.

Assuming that Archie's equation is applicable, the cementation exponent for carbonates is estimated to range between 1.7 and 2.3 (Schön, 2004). Applicability of Archie's equation to carbonates for fully saturated samples has been shown on a sample data set by Glover (2016). Here, we will assume that all samples obey the same Archie's equation, which allows us to derive the bulk resistivity as a function of porosity. We thus assume that

$$log_{10}\left(\frac{\rho_{bulk}}{\rho_{water}}\right) = log_{10}(S^{-n}\Phi^{-m}) = -nlog_{10}(S) - mlog10(\Phi)$$

However, since only the weight percent saturation (S^E) is given, we need to use S^E/ϕ to convert the given weight saturations to pore space saturations. Hence, equation becomes

$$log_{10}\left(\frac{\rho_{bulk}}{\rho_{water}}\right) = \underbrace{-nlog_{10}S^E}_{a_0} + \underbrace{(n-m)}_{b} log_{10}(\Phi).$$

We can fit a line to the porosity/saltwater resistivity values for ρ_w=0.2 Ωm, taking the porosity estimates from volume weight ratios into consideration. a_0 and b are the fitting parameters of the line in Figure S3.

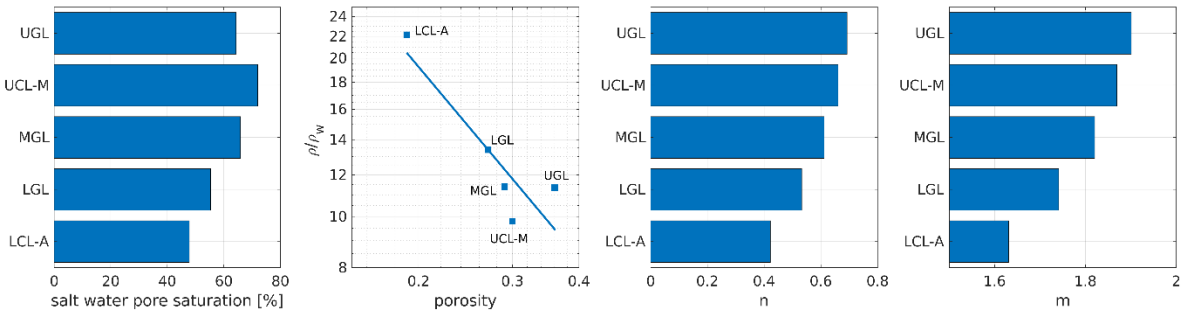

Figure S3: Archie considerations for deriving cementation exponent (m).

Figure S3 shows the linear fits of the data corresponding to the respective values of *m* and *n*. For all samples, we obtain a cementation exponent between 1.6 and 1.9 with a mean at

approximately 1.8. Thus, as a first-order approximation for assessing potential OFG associated resistivity structure in the main text of the manuscript, we use m=1.8. This was also used to create the color shading in the top panel of Figure 3a.

S4. Controlled Source Electromagnetics

A seafloor-towed controlled source electromagnetic (CSEM) experiment was carried out offshore Malta in October 2018 with a modular, electric dipole-dipole system consisting of a 100-m long transmitter dipole followed by three inline receivers at offsets of 150 m, 280 m, and 510 m, respectively (Figure S4). A 50% duty cycle step function was used as a source signal with a period of 4 s and a current amplitude of 20 A (Micallef et al., 2019). Data were acquired along five profiles running perpendicular (lines 2, 6, and 9) and parallel to the coastline (lines 5 and 8) with a total length of ~23 km. CSEM step-on data were processed following the sensitivity analysis study of Haroon et al. (2020) at stationary waypoints every several hundred meters. Final transients and corresponding error estimates were obtained from stacking gain- and drift-corrected time-series and interpreted using a time-domain version of MARE2DEM (Key, 2016; Haroon et al., 2018b). Note that a 5% minimum error was imposed on the data to account for systematic errors caused by

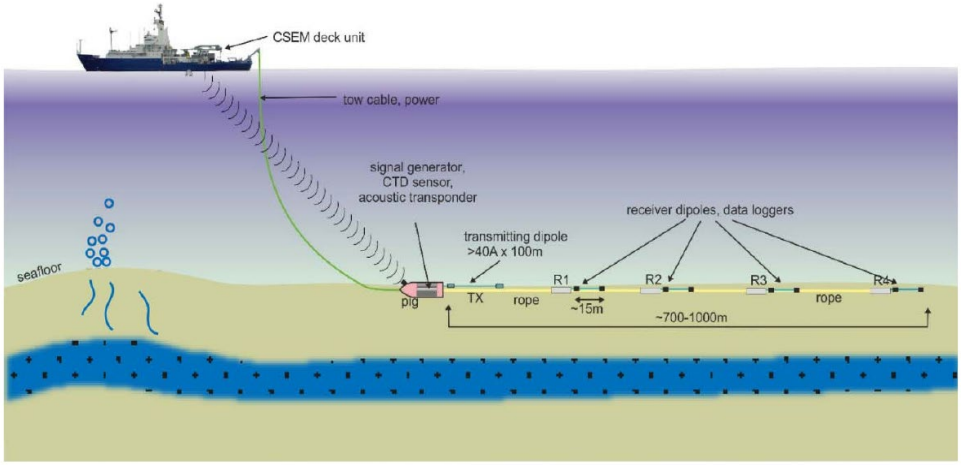

Figure S4: Schematic of seafloor-towed time-domain controlled source electromagnetic system used for groundwater prospecting along Continental shelf regions (Schwalenberg et al., 2017). The system consists of a 100 m long transmitter dipole and several inline electrical field receivers that measure the response of the excited current function at 10 kHz sampling rate.

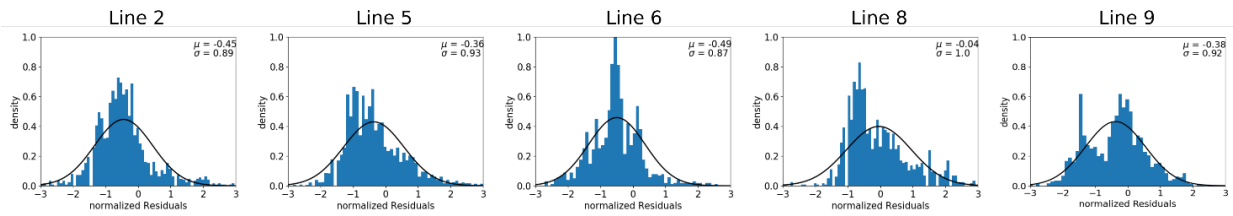

Figure S5: Distribution of the normalized residuals for inversion model presented in Figure 2 of the manuscript. Normalized residuals are shown as histograms. A normal distribution with corresponding mean and standard deviation is displayed by the black line.

inaccurate navigation data. The absolute source normalized noise level obtained by measuring during silent transmitter states varied each measurement day but was on the order of 5e-12 V/m at 1 s.

Data Residuals and Fit from 2D CSEM Inversion

After processing the data, 2D inversion was carried out in the time domain using MARE2DEM (Key, 2016). The resulting best-fit inversion models are displayed in Figure 2 of the manuscript. All models achieved an overall misfit of RMS=1. To better analyze the data misfit structure, Figures S5-S10 show the data characteristics of each inversion model. The distribution of the normalized residuals, defined as the difference between the

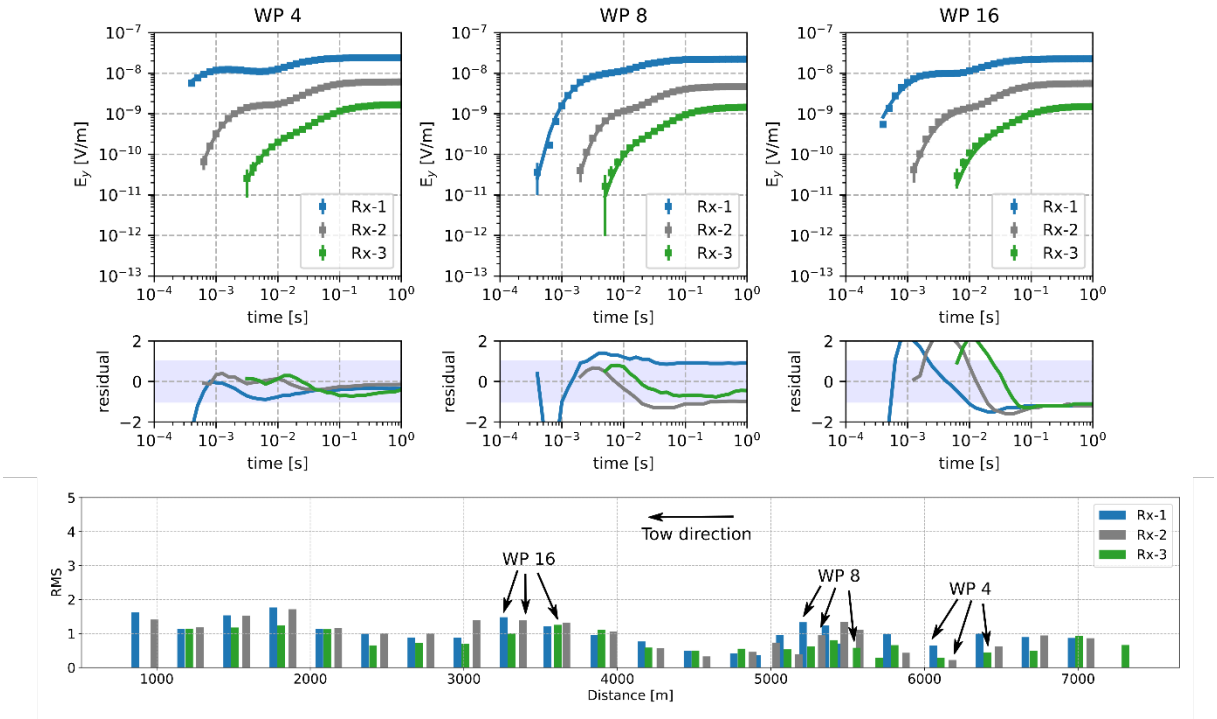

Figure S6: (top) Exemplary data fit for waypoints 4, 8, and 16 along Line 5. Transients corresponding to the nearest (Rx1) to furthest (Rx3) receivers are denoted by blue, gray, and blue colours, respectively. (bottom) RMS values computed for each WP and receiver.

measured and calculated data normalized by the corresponding data error, are displayed for each profile in Figure S5. The data residuals generally show a normal distribution that is biased towards negative residuals along Lines 2, 5, and 6 and towards positive residuals along Line 9. Time-domain data can exhibit a bias within the inversion where measured values are shifted by a constant factor due to improper definition of the measurement geometry, gain, or current amplitude. In these cases, the data fit still arrives at an overall RMS=1 due to the imposed 5% minimum relative error, but is biased towards larger or smaller amplitudes compared to the calculated data. This shift between measured and calculated transients can be observed when inspecting individual transients. In 1D inversion approaches, this shift is accounted for through a calibration factor that shifts the measured data by a specific value to provide a better data fit. Here, we have not used a calibration factor in our 2D inversion and consequently, the residuals are slightly biased. To further investigate the data misfit for individual profiles and transients, Figures S6-S10 show the RMS of each receiver along Lines 2, 5, 6, 8 and 9, respectively along with exemplary transients where RMS values exceeded the mean.

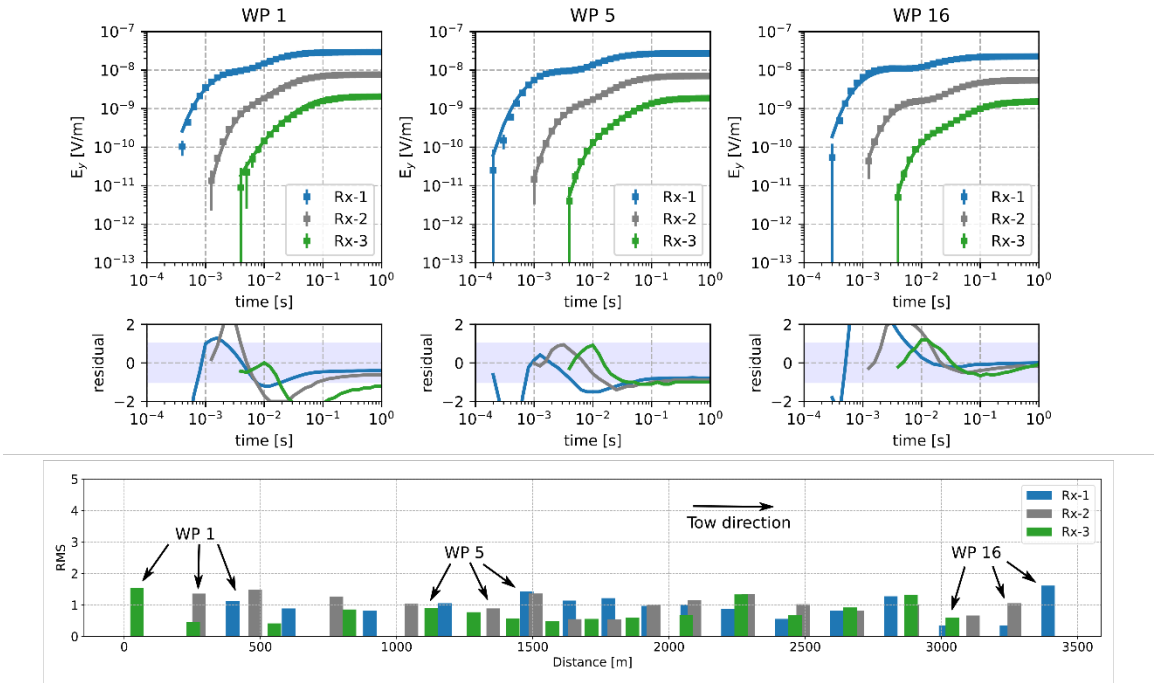

Figure S7: (top) Exemplary data fit for waypoints 1, 5, and 16 along Line 2. Transients corresponding to the nearest (Rx1) to furthest (Rx3) receivers are denoted by blue, gray, and blue colours, respectively. (bottom) RMS values computed for each WP and receiver along the profile.

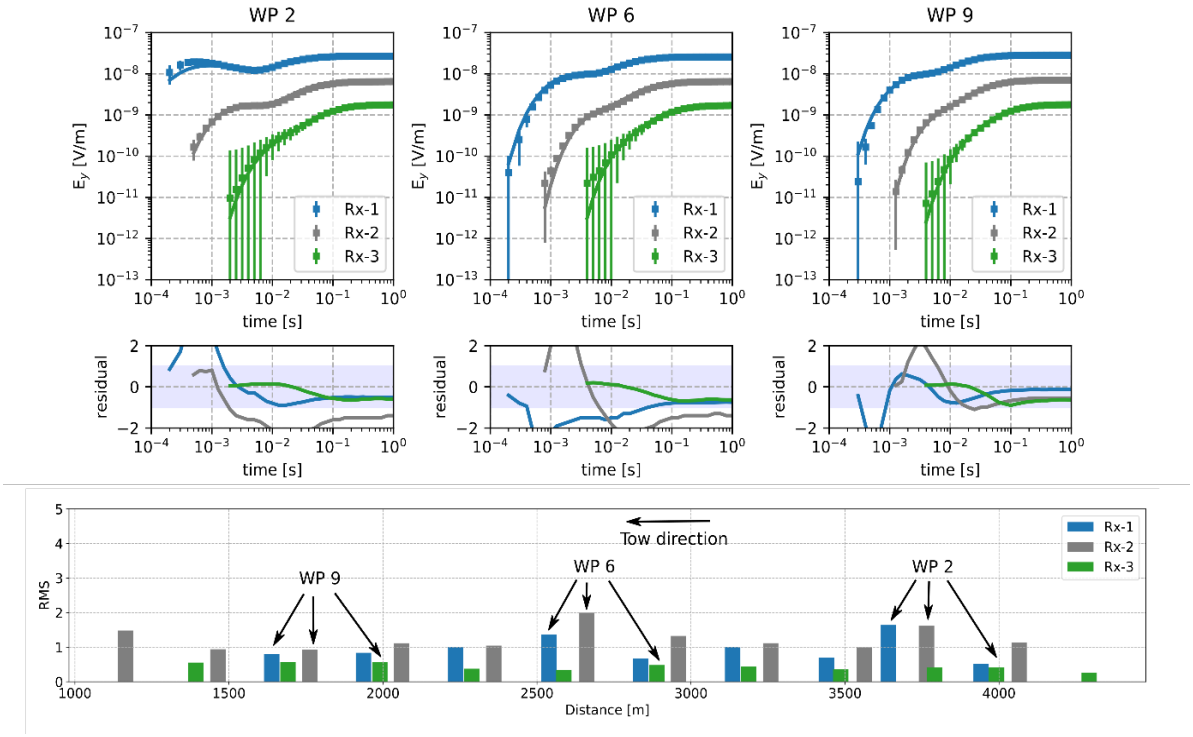

Figure S8: (top) Exemplary data fit for waypoints 2, 6, and 9 along Line 6. Transients corresponding to the nearest (Rx1) to furthest (Rx3) receivers are denoted by blue, gray, and blue colours, respectively. (bottom) RMS values computed for each WP and receiver.

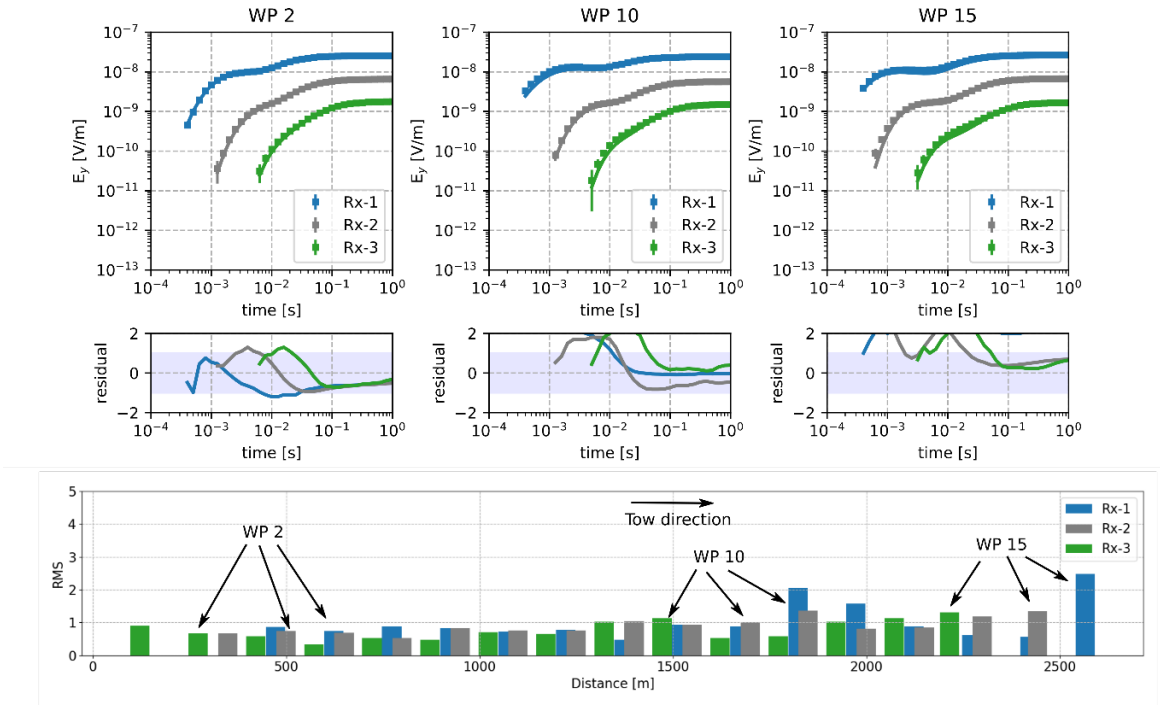

Figure S9: (top) Exemplary data fit for waypoints 2, 10, and 15 along Line 8. Transients corresponding to the nearest (Rx1) to furthest (Rx3) receivers are denoted by blue, gray, and blue colours, respectively. (bottom) RMS values computed for each WP and receiver.

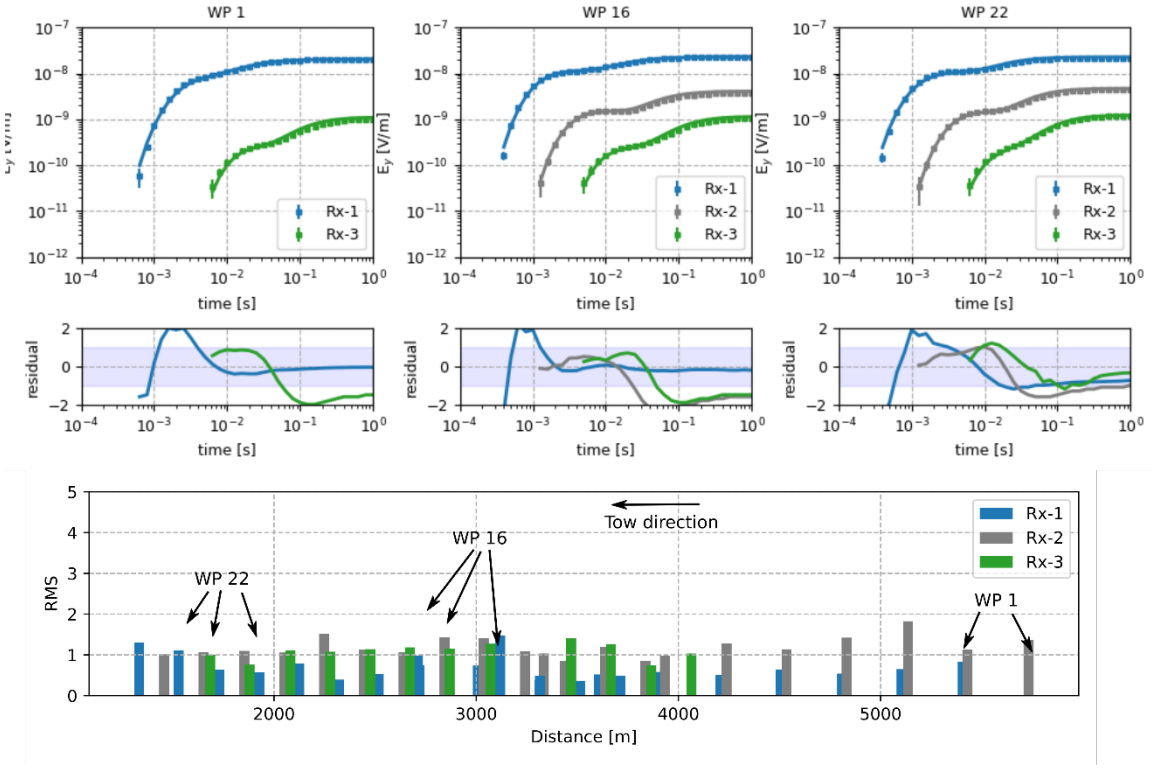

Figure S10: (top) Exemplary data fit for waypoints 1, 16, and 22 along Line 9. Transients corresponding to the nearest (Rx1) to furthest (Rx3) receivers are denoted by blue, gray, and blue colours, respectively. (bottom) RMS values computed for each WP and receiver.

Isotropic versus Transversely Isotropic Inversion

Localized resistivity anomalies are found embedded within the seafloor along Lines 5, 8, and 9. The presented resistivity models in Figure 2 of the manuscript were computed with an isotropic resistivity model. If these local anomalies are associated with vertical electrical anisotropy caused by thin interbedded layers is investigated. Figures S11 and S12 show a comparison between the vertical anisotropic and isotropic inversion models for lines 5 and 9 exemplarily. Overall, the resistivity structure is consistent between the isotropic and transversely isotropic inversion. Along Line 9, the ratio of ρ_z/ρ_y equals a value of approximately one throughout the entire model. Line 5 also shows consistent ρ_z/ρ_y ratios aside from the paleo-channel infill labelled C1 in Figure 2c. Consequently, we conclude that the isotropic models are a sufficient representation of the subsurface resistivity structure without introducing artefacts caused by vertical electrical isotropy.

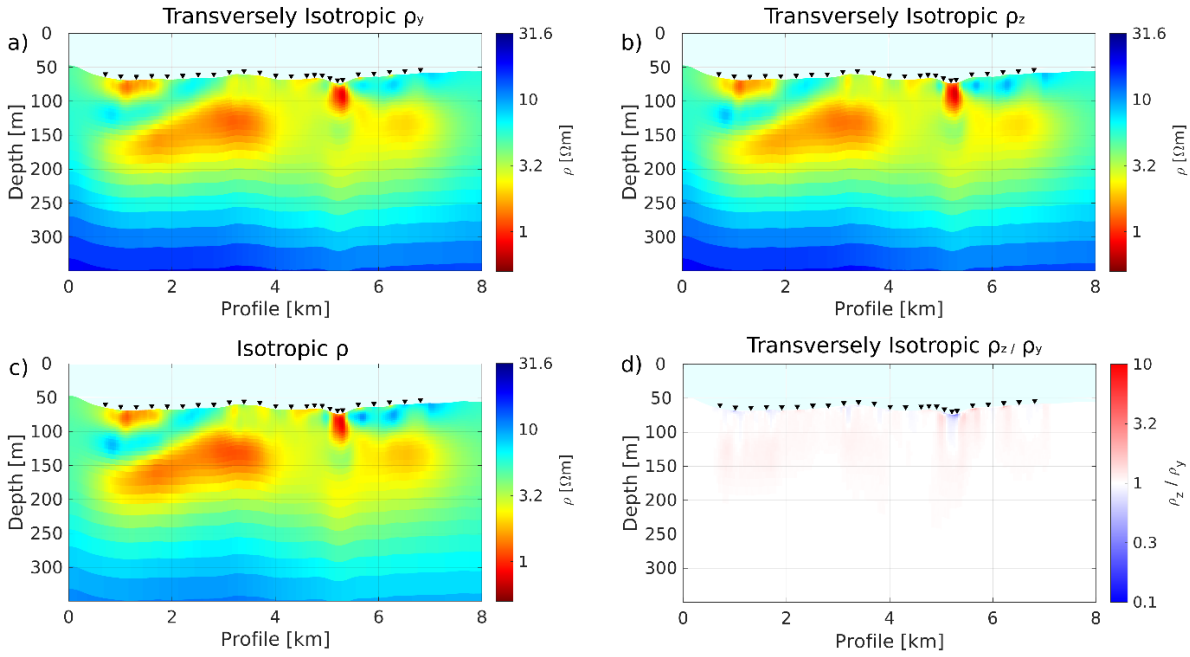

Figure S11: Comparison between the transversely isotropic and isotropic 2D CSEM inversion along Line 5. (a) ρ_y, (b) ρ_z and (d) ratio of ρ_z/ρ_y for vertical anisotropic inversion. (c) Isotropic inversion model as displayed in Figure 2 of the manuscript for comparison. The black triangles mark the transmitter waypoints along each profile.

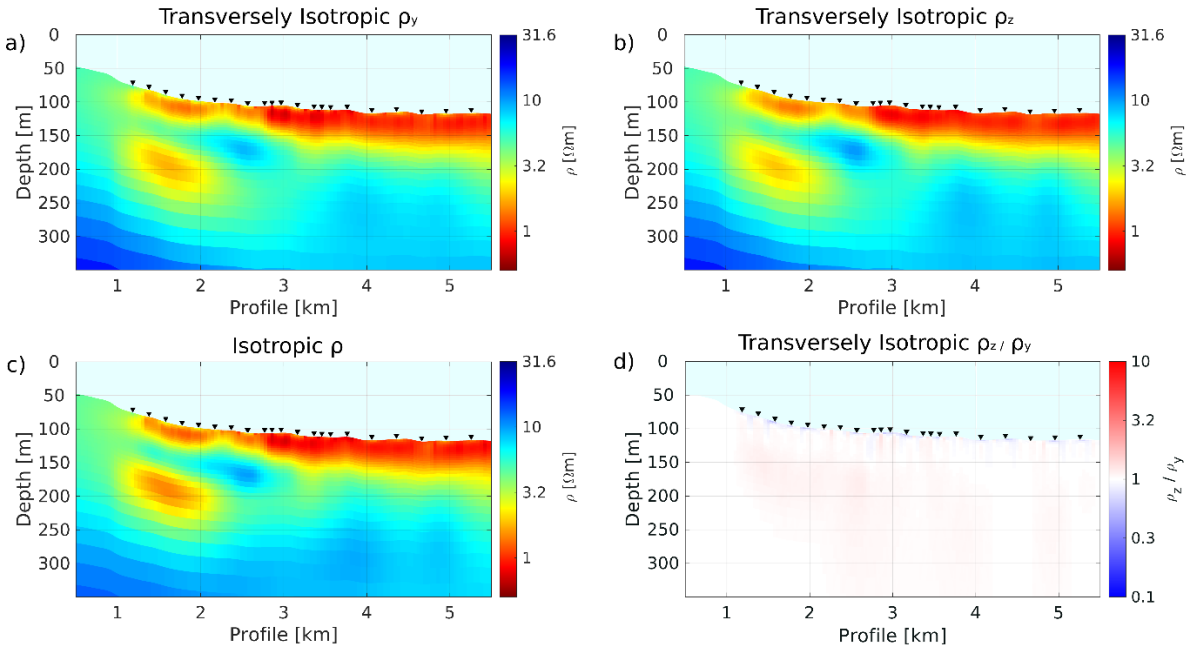

Figure S12: Comparison between the transversely isotropic and isotropic 2D CSEM inversion along Line 9. (a) ρ_y, (b) ρ_z and (d) ratio of ρ_z/ρ_y for vertical anisotropic inversion. (c) Isotropic inversion model as displayed in Figures 2 and 3 of the manuscript for comparison. The black triangles mark the individual waypoints along each profile.

Synthetic CSEM modelling and inversion

R1 is a prominent resistive feature found directly underneath the seafloor along line 6 in the CSEM inversion models. Synthetic modeling studies were conducted to assess if the

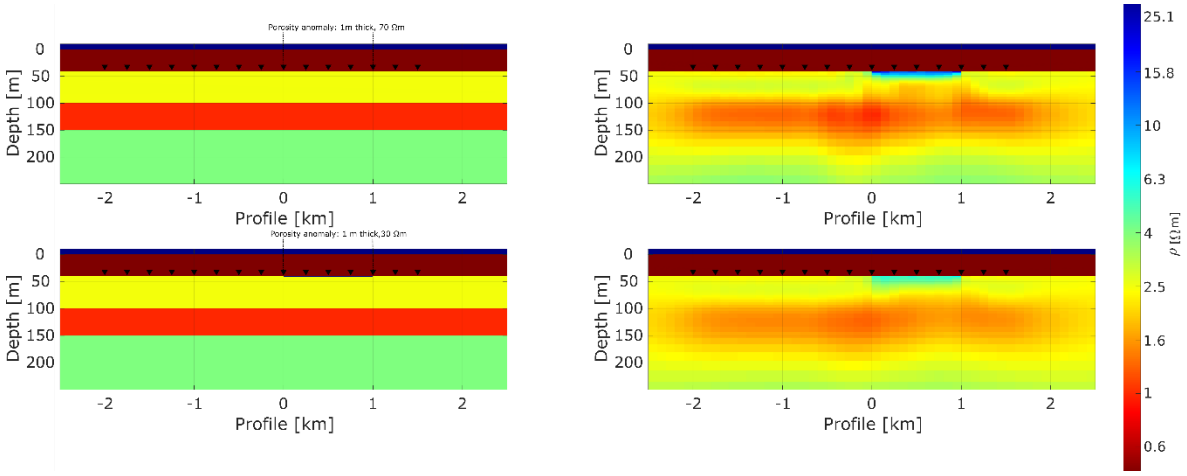

Figure S13: Synthetic modelling study to investigate the resolution capabilities of the applied CSEM system to resolve shallow resistive structures. (left) Forward models with an anomalous resistive layer of (top) 70 Ωm and (bottom) 30 Ωm. The corresponding inversion models are depicted in the right column.

applied CSEM system can resolve such shallow resistivity structure. Figure S13 shows this forward and inversion modelling study using the corresponding error model of the measured data. To achieve a similar feature as R1, a 1 m thick resistive body must have a resistivity of around 70 Ωm. Even for lower resistivities of around 30 Ωm, the CSEM system is able to pick up the feature, but inversion models show slightly lower resistivities to what is observed along line 6.

S5. Seismic Sections with interpreted geological model

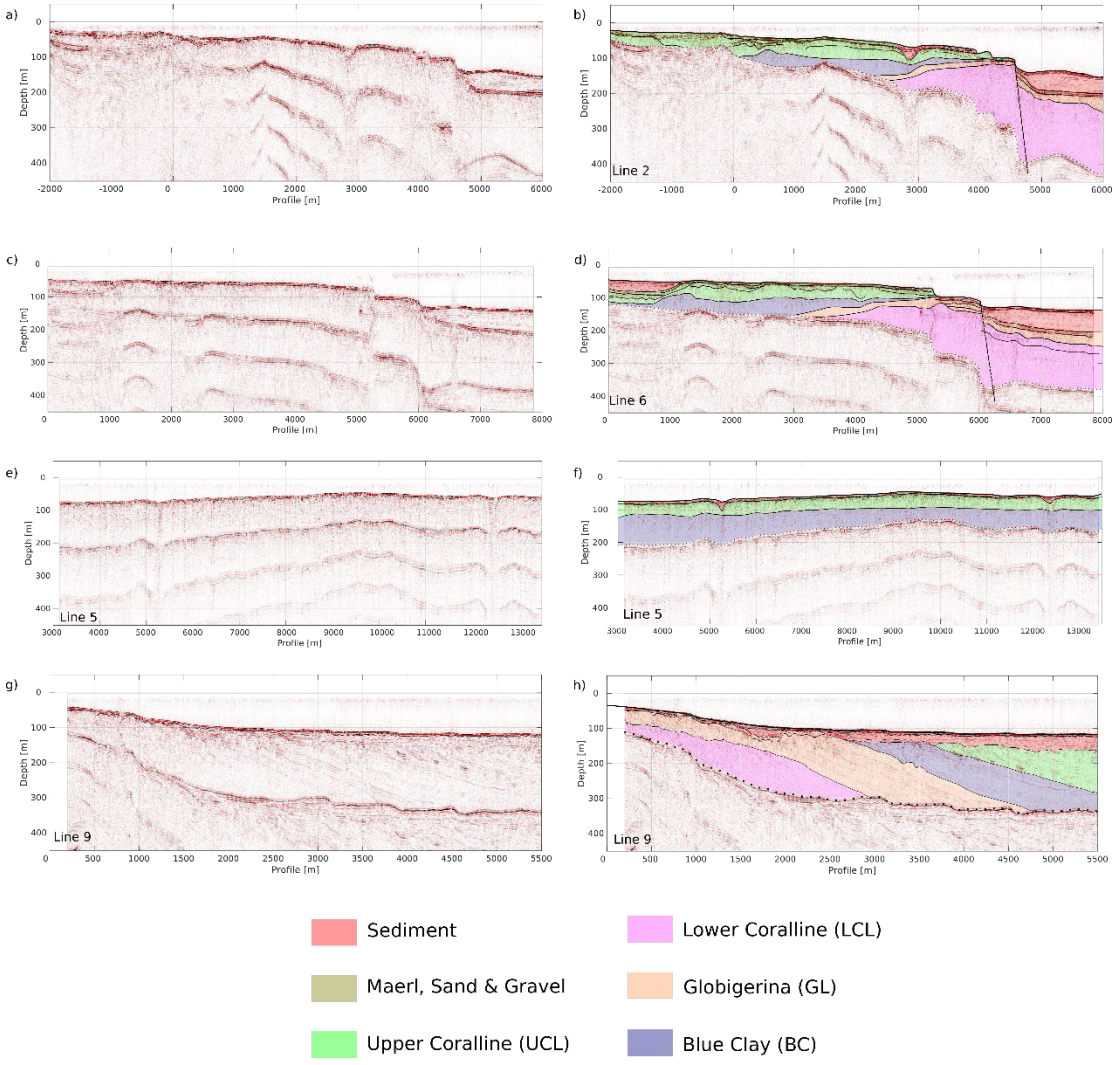

Figure S14: Uninterpreted (left) and interpreted (right) seismic reflection profiles shown in Figure 2. The dotted line in the interpreted sections marks the arrival of the first seafloor multiple which masks information at greater depth. Different coloured shading corresponds to the inferred lithological units described in the main text of the manuscript and explicitly marked in Figure 2.

Four collocated 2-D seismic reflection profiles were acquired during a two-day survey in October 2018. We used a single mini-GI gun with two chambers of 30 cubic inches each. The gun was operated with two diving compressors at 120-130 bar. The resulting data were recorded with a Geometrics Geo-eel solid state streamer that consisted of four sections. Each section is 12.5 m long and has eight hydrophone groups yielding 32 channels. Navigation was based on a dedicated GPS antenna mounted on the bridge deck. The shot interval was about 10 m, depending on surface currents.

The seismic processing included the streamer geometry configuration using in house Unix/Fortran scripts. Delay calculations and source and receiver depth control as well as further processing steps were carried out using the Linux-based Seismic Unix processing package. From the seismic data a delay of -27 ms and -35 ms. A receiver ghost effect in the seismic data could not be detected. The source-receiver locations were binned with a common-midpoint bin spacing of 1.5625 m. Different filter tests were performed and the frequency spectra were analyzed. Seismic traces were balanced and filtered using a bandpass filter with corner frequencies at 30, 50, 60, 420, 500 Hz. The traces were balanced with a rms normalizing window starting at 0.05 s. Subsequently, a normal move out correction (with a constant velocity of 1500.00 m/s) and stacking were applied. The stack was migrated with a 2D Stolt algorithm 1500 m/s constant velocity model.

The uninterpreted and interpreted seismic sections are displayed in the left and right columns of Figure S14, respectively. Lithological formations were identified in borehole data labelled BH3 in Figures 1 and 2 of the manuscript and extrapolated across Line 2 using distinct reflections in the seismic cross-sections. Interpretations are terminated at the onset of the first multiple (dotted lines). Additionally, Line 9 was correlated with seismic data from Gatt (2012) to identify the reflectors corresponding to the lower boundary of the Globigerina Limestone formation.

S6 Hydrogeological modeling

Simulations were conducted along line 9 and its onshore extension to assess if, and under which conditions, freshened groundwater would occur offshore SE Malta. The cross-section is oriented in the general direction of groundwater flow, which is perpendicular to

the coast. The model includes a portion of the island up to a distance of 2.2 km from the shoreline and extends 5.2 km offshore. The variable density groundwater model SEAWAT (Langevin et al., 2008) was used to run the simulations under transient conditions.

Spatial discretization

The simulation domain has an overall length of 7.4 km and a maximum height of 560 m (Figure S15). The bottom of the model is set at a depth of 500 m below sea level, which is significantly deeper than the freshwater–saltwater interface. The simulation domain is vertically discretized with layers tracing the structure of the existing geological formations. The thicker layers have been further subdivided to facilitate the convergence of the solute transport equation (Zheng, 1990). The domain has been horizontally discretized by dividing each layer with 200 elements (Figure S15).

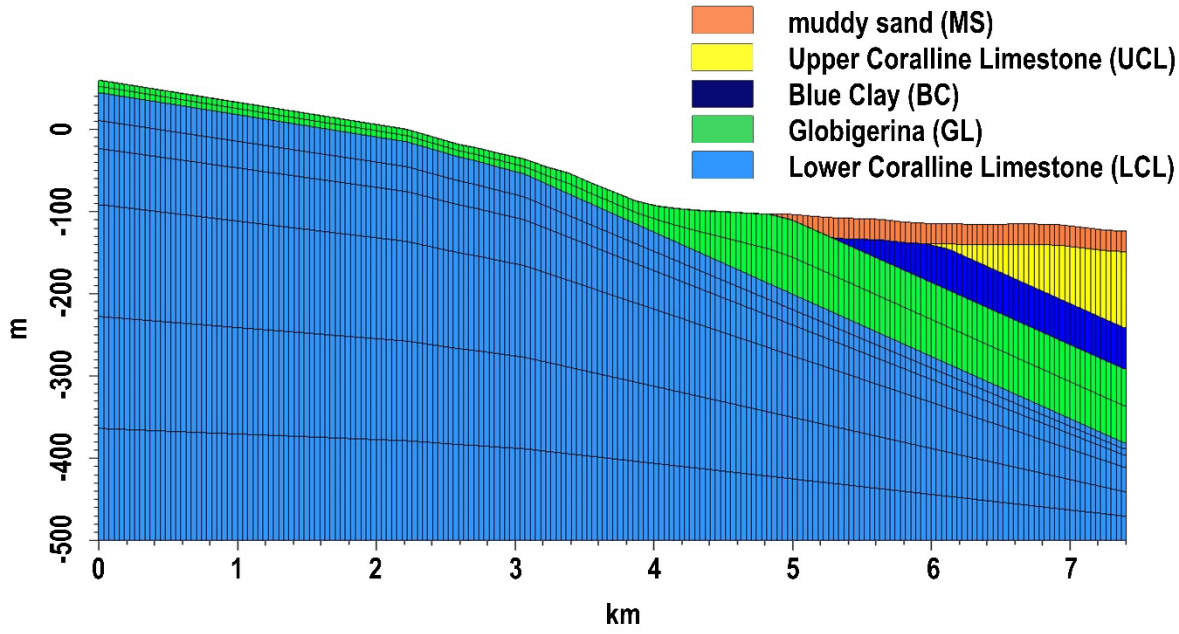

Figure S15. *Model domain showing discretization settings and geological formations.*

Aquifer and fluid properties

Aquifer hydraulic properties in the model are assigned according to the values shown in Table A2. The specific yield was set to be equal to the porosities of the lithological units, whereas the specific storage was derived from the literature (Kuang et al. 2020).

Table S2. Hydraulic conductivity and porosity of the geological formations of the Maltese Island.

Formation	UCL	BC	GL	MS	LCL
Hydraulic Conductivity [m/s]	4.9×10^{-5}	1.2×10^{-8}	8×10^{-6}	2.3×10^{-6}	1.0×10^{-4}
Porosity [-]	0.30	0.35	0.30	0.25	0.19
Specific Storage [1/m]	3.8×10^{-6}	4.4×10^{-6}	3.8×10^{-6}	3.1×10^{-6}	2.4×10^{-6}

Source: (Stuart et al., 2010; Cassar, 2010; Cooke et al., 2018; Gatt, 2012; Bakalowicz and Mangion, 2003; Sapiano et al., 2017a, b; Fusi and Castellanza, 2019; Environment and Resources Authority, 2015, Verweij et al., 2016; Henri et al., 2019).

The aquifer is considered as unconfined and each geological formation is modeled as homogeneous. There are no layers of impermeable material located both above and below the aquifer that cause it to be under pressure. The water table is at atmospheric pressure, and can thus rise and fall as a result of external forcings. The model layers are set to be "convertible", which means that the model checks the hydraulic head value of each cell to determine if it is confined or not. Cells in convertible layers are either confined or unconfined depending on whether the head is above or below the top of the cell. Three different factors of anisotropy of hydraulic conductivities (K_h/K_v of 1, 10 and 100) are investigated to assess its influence on OFG extension. The longitudinal dispersivity, which is used to represent the local variations in the velocity field of a groundwater solute in the direction of fluid flow, has been estimated using the empirical power law developed by Schulze-Makuch (2005):

$$\alpha = c(L)^m$$

where α is longitudinal dispersivity [L], c a parameter characteristic for a geological medium [L^{1-m}], L the flow distance [L], and m the scaling exponent. These parameters have been quantified for unconsolidated sediments and consolidated rocks via the analysis of hundreds of data pairs. In the present study, the aforementioned factors have been derived

for carbonate rocks and a modeling scale of 10 km. The resulting longitudinal dispersivity is equal to 30 m and the transversal one is set to be a tenth.

The density of seawater is set to 1.025 g/cm^3 for a salt concentration of 35 g/l while the density of freshwater is set to 1 g/cm^3 (0 g/l salt concentration).

Boundary conditions

The aquifer bottom (B-C in Figure S16) is an impervious boundary for flow and transport. The seaward boundaries C-D and D-E are assumed to be at seawater hydrostatic pressure. On these boundaries, we specify the saltwater heads and a prescribed concentration equal to 35 g/l. A specified freshwater hydraulic head is applied at the lateral inland boundary (A-B).

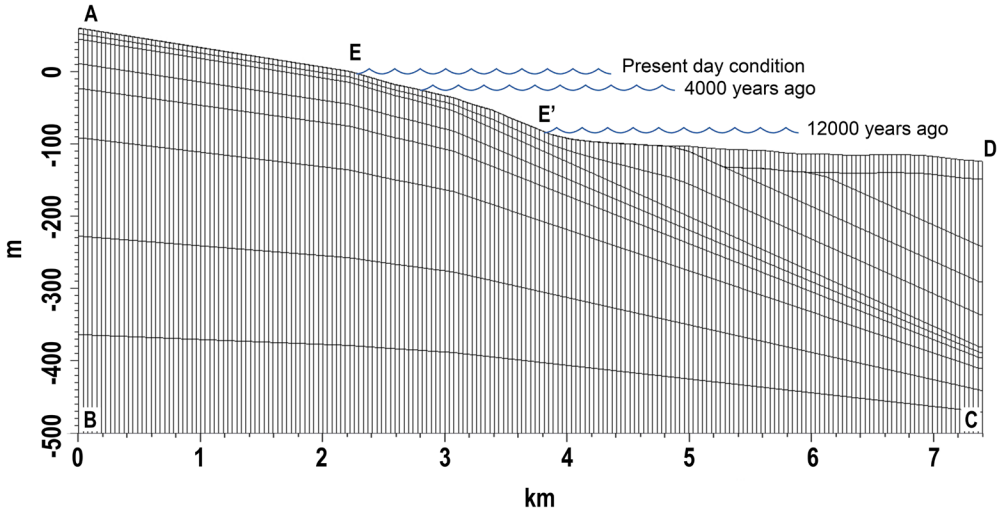

Figure S16. *Schematic boundary condition evolution for sea-level rise simulations.*

Simulation strategy

Simulations started from 20 ka ago with an initial salt concentration of 0 g/l in the aquifer, when sea level reached the value of -130 m (point D of Figure S16) during the Last Glacial Maximum (Caruso et al., 2011; Lambeck et al., 2011). This represented the largest exposure of the Maltese Islands, with the paleo-coastline at 7 km to the east of the present coastline (Micallef et al., 2013). The water table is assumed to have been in equilibrium

with a sea-level at -130 m and extended to the paleo-coastline. At this point, the aquifer is at its maximum areal expansions and involves all the lithological formations located above the aforementioned equilibrium depth. Sea-level was gradually changed from -130 m to 0 over the past 20 ka. Since the Last Glacial Maximum, sea level rise associated with climatic amelioration during the transition into the current interglacial has drowned the paleolandscape at an average rate of 5 mm per year (Lambeck et al., 2011). This sea-level rise has been modelled as a progressive modification of the sea-bottom boundary condition that accounts for the inland displacement of the coastline. Figure S16 is a schematic representation of the sea-bottom boundary condition evolution where the coastline (E') is displaced progressively inland (E). In the model, the E' location is updated every thousand years and all the cells, along the D-E' boundary, are set as prescribed heads with the transport condition described previously. At the same time, all the elements on the A-B boundary are set to a new specified freshwater hydraulic head. Due to the lack of information on past aquifer conditions, the present-day hydraulic gradient was kept constant for all simulations. In this way, when the saltwater head was specified for a specific simulation, the corresponding freshwater head was determined and set at the inland boundary. Cells and boundary conditions affected by the imposed sea-level rise were updated twenty times during the simulation period. This means that twenty successive simulations, each of which used results from the previous simulation as the initial condition, were run for the three anisotropy factors imposed to the model.

Results

Figures S17-A19 show the results of the model simulations for anisotropies of 1, 10 and 100, respectively. Each figure displays the modelled groundwater salinity at four different time steps: 15 ka, 10 ka, 5 ka ago and present- day conditions. The evolution from the initial freshwater conditions to the final results entails a progressive salinization, with the formation of an isolated OFG preserved in the low permeability units. The overall groundwater salinity tends to decrease with an increase in the anisotropy, whereas its offshore extension is proportional with the latter. The OFG close to the coast is hosted in LCL and connected to the onshore groundwater system.

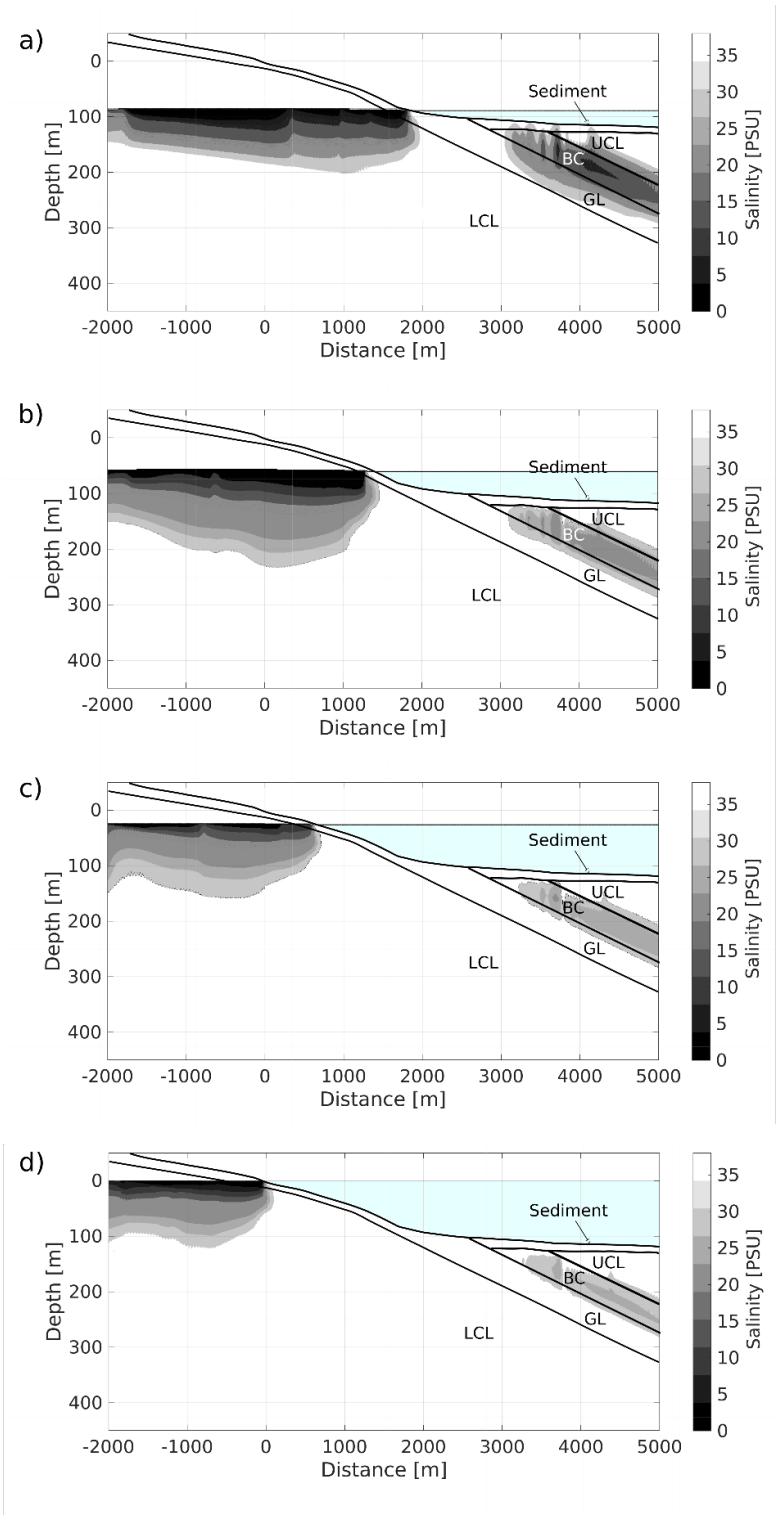

Figure S17. *Modelled groundwater salinity (in PSU) for an anisotropy factor of 1, at four different time steps: a) 15 ka BP, b) 10 ka BP, c) 5 ka BP and d) present- day conditions. The blue-shading denotes the seawater column for the respective time window.*

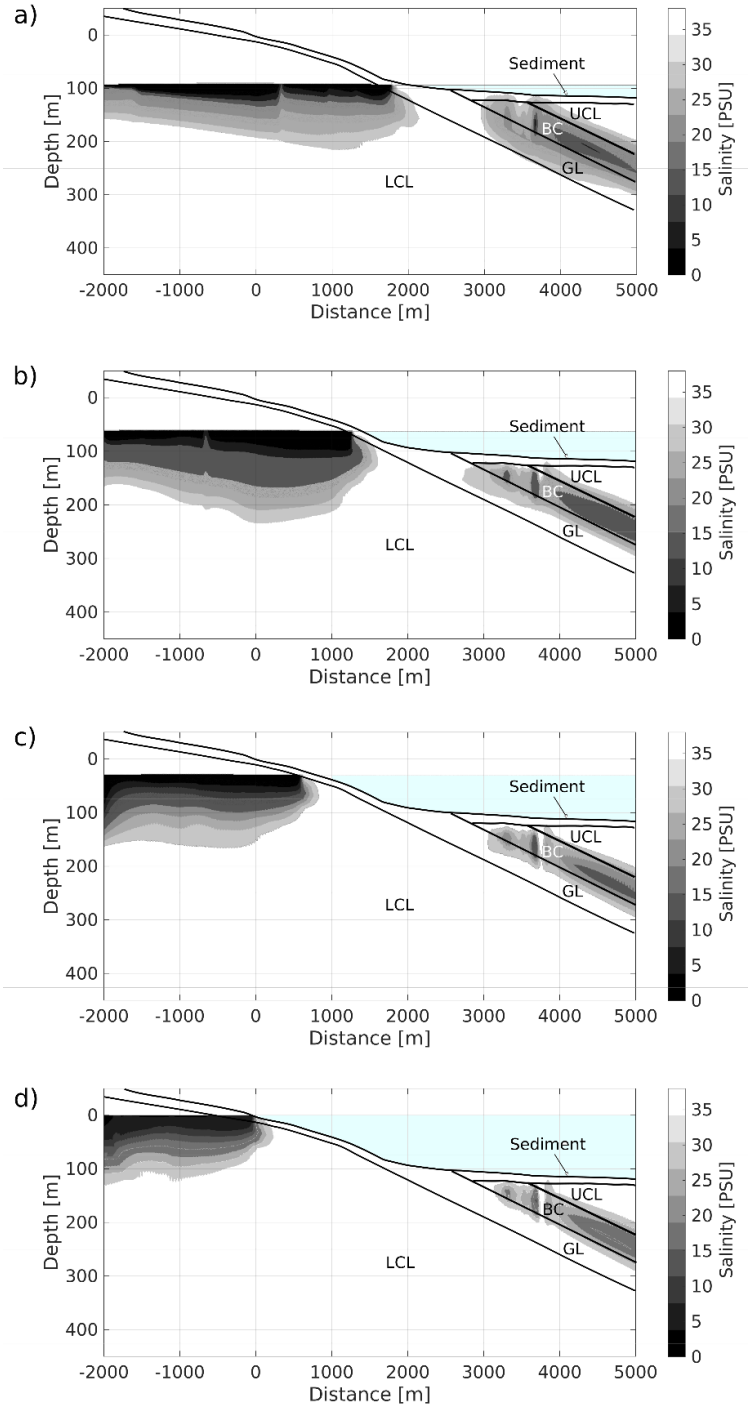

Figure S18. *Modelled groundwater salinity (in PSU) for an anisotropy factor of 10, at four different time steps: a) 15 ka BP, b) 10 ka BP, c) 5 ka BP and d) present- day conditions. The blue-shading denotes the seawater column for the respective time window.*

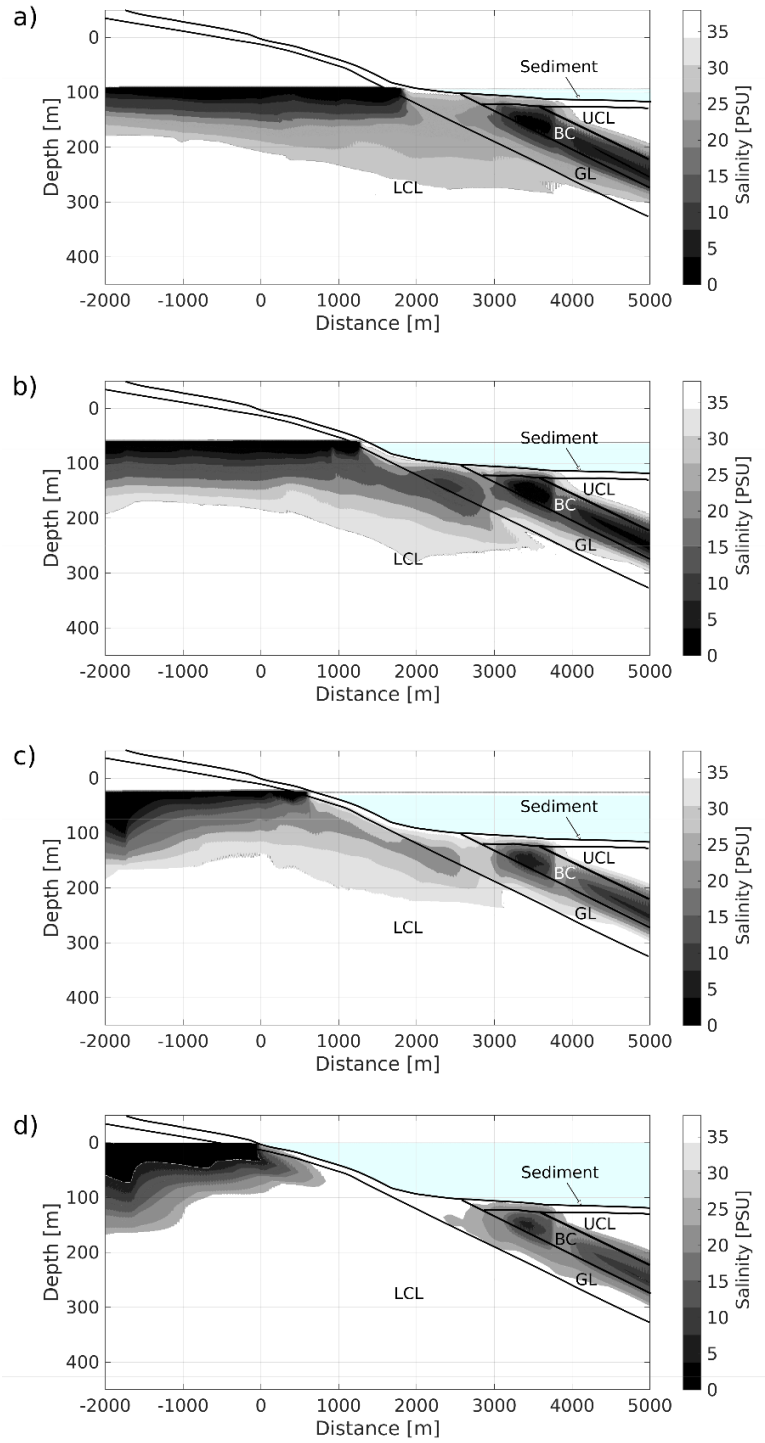

Figure S19. *Modelled groundwater salinity (in PSU) for an anisotropy factor of 100, at four different time steps: a) 15 ka BP, b) 10 ka BP, c) 5 ka BP and d) present- day conditions. The blue-shading denotes the seawater column for the respective time window.*